Coupled superconducting qudit-resonator system: Energy spectrum, state population, and state transition under microwave drive

W. Y. Liu,[1,2] H. K. Xu,[1,2] F. F. Su,[1,2] Z. Y. Li,[1,3] Ye Tian,[1] Siyuan Han,[4,1] and S. P. Zhao[1,2,5]

[1]*Beijing National Laboratory for Condensed Matter Physics, Institute of Physics, Chinese Academy of Sciences, Beijing 100190, China*
[2]*School of Physical Sciences, University of Chinese Academy of Sciences, Beijing 100049, China*
[3]*School of Physics, Nanjing University, National Laboratory of Solid State Microstructures, Nanjing 210093, China*
[4]*Department of Physics and Astronomy, University of Kansas, Lawrence, Kansas 66045, USA*
[5]*CAS Center for Excellence in Topological Quantum Computation, University of Chinese Academy of Sciences, Beijing 100190, China*

Superconducting quantum multilevel systems coupled to resonators have recently been considered in some applications such as microwave lasing and high-fidelity quantum logical gates. In this work, using an rf-SQUID type phase qudit coupled to a microwave coplanar waveguide resonator, we study both theoretically and experimentally the energy spectrum of the system when the qudit level spacings are varied around the resonator frequency by changing the magnetic flux applied to the qudit loop. We show that the experimental result can be well described by a theoretical model that extends from the usual two-level Jaynes-Cummings system to the present four-level system. It is also shown that due to the small anharmonicity of the phase device a simplified model capturing the leading state interactions fits the experimental spectra very well. Furthermore we use the Lindblad master equation containing various relaxation and dephasing processes to calculate the level populations in the simpler qutrit-resonator system, which allows a clear understanding of the dynamics of the system under the microwave drive. Our results help to better understand and perform the experiments of coupled multilevel and resonator systems and can be applied in the case of transmon or Xmon qudits having similar anharmonicity to the present phase device.

I. INTRODUCTION

Superconducting qubit and resonator systems [1] are the key elements of superconducting quantum circuits which have wide applications in solid-state quantum computing [2–4] and quantum simulation [5]. For example, quantum nondemolition measurements of the qubit state can be realized via a coupled three-dimensional resonator or one-dimensional transmission line resonator whose transmission/reflection characteristics depend critically on the qubit state [6–8]. The coupled qubit and resonator systems, due to their unique properties, have also emerged as fundamental building blocks of the superconducting quantum simulators for the studies of a number of model Hamiltonians in condensed-matter physics, ranging from quantum Ising chains [9,10], Holstein polarons [11], to Mott insulator-superfluid quantum phase transitions [12].

In addition to the qubits, superconducting three-level systems, namely, qutrits, have been used in many quantum optics studies [13] such as Autler-Townes splitting (ATS), electromagnetically induced transparency (EIT), and coherent population transfer [14–20]. These processes have the potential for building devices like photon filters, routers, and switches in various superconducting quantum circuit applications [16,21]. It is interesting to note that ATS and EIT have also been investigated in the coupled qubit and resonator systems in which the dressed states of the coupled system are adopted [22,23].

Recently there are many studies in which the coupled qutrit- and qudit (i.e., a four-level device) -resonator systems are involved [24–29]. Yang *et al.* discussed the generation of entangled states in the qutrit-resonator system [24]. Peng and *et al.* realized experimentally the two-mode correlated emission lasing in resonators coupled via a fully controllable superconducting flux qutrit [25]. Hua *et al.* proposed a controlled phase gate having high fidelity and short operation time with two superconducting resonators coupled to a transmon qutrit [26]. The circuit-QED implementations of controlled phase gate [27] and heralded near-deterministic controlled Toffoli gate [28] were also proposed based on superconducting qudits coupled to the resonator. Furthermore, the creation of N-photon NOON states was realized in the multicoupled qutrit-resonator system [29]. Note that also more than the qubit two levels (or qutrit three levels) are found necessary in explaining the experiments such as ATS [15], geometric phase realization [30], and a protocol for demonstrating quantum supremacy [31], and quantum state leakage and transition out of the qubit subspace are encountered in both the qubit [32] and qubit-resonator [33] systems. In all these cases, it is imperative to have an accurate description of the energy spectrum of the coupled superconducting qutrit- and qudit-resonator systems when their level spacings are varied in the vicinity of the resonator frequency, as well as the state population and transition in response to the microwave driving. So far, a detailed theoretical treatment and its comparison with experiment are still lacking.

In this work, we investigate, both theoretically and experimentally, the energy spectrum of the coupled superconducting four-level qudit-resonator system (the three-level qutrit-resonator system is naturally included). We use an rf-SQUID
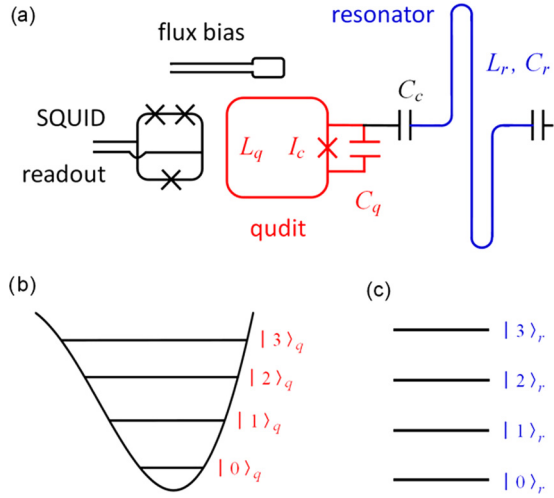
FIG. 1. (a) Schematic of the coupled rf-SQUID type phase qudit (red) and resonator (blue) system. The qudit has a Josephson critical current I_c, shunt capacitance C_q, and loop inductance L_q while the resonator is characterized by its effective inductance L_r and capacitance C_r. They are coupled by a capacitance C_c. The flux bias provides both dc and rf components of $\Phi_{ext} = \Phi_{dc} + \Phi_{rf}(t)$. (b) Energy potential and level diagram of a superconducting phase qudit. (c) Energy-level diagram of a resonator.

type phase qudit so its level spacings can be conveniently tuned by changing the applied magnetic flux bias [see Fig. 1(a)]. The experimental spectra are measured with increasing microwave power so that multiphoton processes are involved and populations up to the third-excited level are detected [see Fig. 1(b)]. We show that the calculated energy spectra from a theoretical model taking account of the multilevel structure of the qudit-resonator system agree well with the experimental results. We then consider a simplified model based on the small anharmonicity of the phase type device, which provides a straightforward picture of the state interactions and also a good fit to the experimental data. Furthermore, we use the Lindblad master equation containing various relaxation and dephasing processes to calculate the population at each energy level of the qutrit-resonator system, which allows a clear understanding of the dynamics of the system under microwave driving. Finally, we present examples that our results can help to better understand and perform some experiments of the coupled multilevel and resonator systems.

In the following, we will first present our theoretical formulation (Sec. II) and a description of the experiment (Sec. III), followed by the results and discussions of the experiment and numerical calculations (Sec. IV). The final section V summarizes our main findings.

II. THEORY

The Hamiltonian of the coupled qudit-resonator system subject to a microwave field [see Fig. 1(a) for the definition of various system parameters] can be written as

$$
\begin{aligned}
H &= H_q + H_r + H_c \\
&= H_q^0 - \Phi_q \Phi_{rf}(t)/L_q + H_r + H_c \\
&= H_0 - \Phi_q \Phi_{rf}(t)/L_q,
\end{aligned}
\tag{1}
$$

with the subscripts q, r, and c denoting the qudit, the resonator, and their coupling, respectively. In Eq. (1), Φ_q is the qudit's flux variable and we separate the time-dependent microwave drive $\Phi_{rf}(t) = A \cos(\omega t)$ term of $-\Phi_q \Phi_{rf}(t)/L_q$ from H_q so that in the absence of microwave drive the qudit-resonator system's Hamiltonian $H_0 = H_q^0 + H_r + H_c$ is time independent.

Details of the derivation and further discussion are presented in Appendix A. In short, by introducing the creation and annihilation operators for the qudit, its Hamiltonian H_q^0, which has an anharmonic cubic potential, can be written as ($\hbar = 1$ will be used hereafter for simplicity)

$$
H_q^0 = \omega_q\left(a_q^\dagger a_q + \tfrac{1}{2}\right) + \eta(a_q^\dagger + a_q)^3,
\tag{2}
$$

where ω_q is the Josephson plasma frequency and η is a small quantity compared to ω_q. H_q^0 can be diagonalized to obtain the qudit energy levels E_n corresponding to the eigenstates $|n\rangle_q$ ($n = 0, 1, 2, \ldots$), as shown in Fig. 1(b). Similarly, the Hamiltonian of the resonator can be written as

$$
H_r = \omega_r\left(a_r^\dagger a_r + \tfrac{1}{2}\right),
\tag{3}
$$

where ω_r is the resonator frequency, with the energy levels $\epsilon_n = \omega_r(n + 1/2)$ corresponding to the Fock states $|n\rangle_r$ ($n = 0, 1, 2, \ldots$) as shown in Fig. 1(c). Finally the interaction Hamiltonian reads

$$
H_c = g(a_q^\dagger a_r + a_r^\dagger a_q),
\tag{4}
$$

where g is the qudit-resonator coupling strength.

The total Hamiltonian $H_0 = H_q^0 + H_r + H_c$ of the qudit-resonator system, without the microwave drive, is written in Eq. (A10) in the matrix form in the subspace spanned by bases $\{|00\rangle, |01\rangle, |10\rangle, |02\rangle, |11\rangle, |20\rangle, |03\rangle, |12\rangle, |21\rangle, |30\rangle\}$, where $|mn\rangle \equiv |m\rangle_r |n\rangle_q$. We note that all of the nonzero off-diagonal elements in Eq. (A10) contain the parameter $\alpha = \eta/\omega_q$. For the qudit with small anharmonicity, we have $\alpha \ll 1$, so the system Hamiltonian H_0 in Eq. (A10) is approximated as
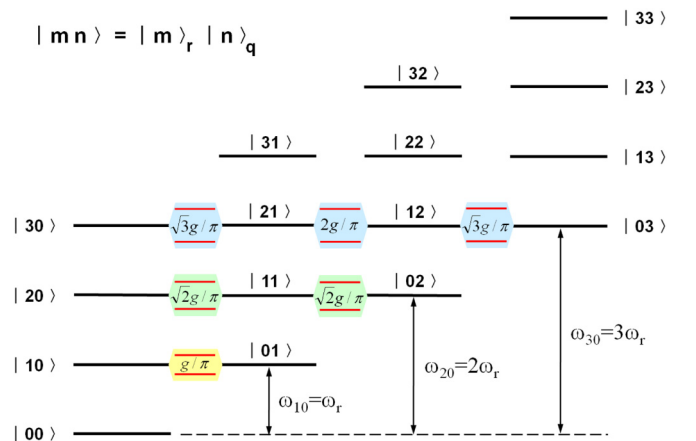

FIG. 2. Energy-level diagram of the coupled qudit and resonator system. The levels are shown for three different resonant cases of $\omega_{10} = \omega_r$ (one-photon), $\omega_{20} = 2\omega_r$ (two-photon), and $\omega_{30} = 3\omega_r$ (three-photon), respectively.

$\alpha \rightarrow 0$ to be

$$
H'_0 = \begin{bmatrix}
\epsilon_0 + E_0 & 0 & 0 & 0 & 0 & 0 & 0 & 0 & 0 & 0 \\
0 & \epsilon_0 + E_1 & g & 0 & 0 & 0 & 0 & 0 & 0 & 0 \\
0 & g & \epsilon_1 + E_0 & 0 & 0 & 0 & 0 & 0 & 0 & 0 \\
0 & 0 & 0 & \epsilon_0 + E_2 & \sqrt{2}g & 0 & 0 & 0 & 0 & 0 \\
0 & 0 & 0 & \sqrt{2}g & \epsilon_1 + E_1 & \sqrt{2}g & 0 & 0 & 0 & 0 \\
0 & 0 & 0 & 0 & \sqrt{2}g & \epsilon_2 + E_0 & 0 & 0 & 0 & 0 \\
0 & 0 & 0 & 0 & 0 & 0 & \epsilon_0 + E_3 & \sqrt{3}g & 0 & 0 \\
0 & 0 & 0 & 0 & 0 & 0 & \sqrt{3}g & \epsilon_1 + E_2 & 2g & 0 \\
0 & 0 & 0 & 0 & 0 & 0 & 0 & 2g & \epsilon_2 + E_1 & \sqrt{3}g \\
0 & 0 & 0 & 0 & 0 & 0 & 0 & 0 & \sqrt{3}g & \epsilon_3 + E_0
\end{bmatrix}. \quad (5)
$$

Equation (5) captures the most fundamental interactions among the basis states of the system as shown in Fig. 2, which will be discussed below.

For the master equation simulation, we take into account the time-dependent Hamiltonian $H' = H'_0 - \Phi_q \Phi_{\text{rf}}(t)/L_q$. For simplicity and without loss of generality, the simpler qutrit-resonator system with 6×6 Hamiltonian matrix spanned in the

smaller subspace spanned by $|00\rangle$, $|01\rangle$, $|10\rangle$, $|02\rangle$, $|11\rangle$, $|20\rangle$ will be considered, whose detailed discussion is given in Appendix B. Denoting various qutrit-microwave and resonator-microwave detunings as $\Delta_p = \omega_{10} - \omega$, $\Delta_c = \omega_{21} - \omega$, $\Delta_r = \omega_r - \omega$, where $\omega_{ij} = E_i - E_j$ is the qutrit level spacings, and performing a rotating-wave approximation to drop terms oscillating with frequency 2ω, we arrive at

$$
H^{\text{RWA}} = \begin{bmatrix}
0 & \Omega/\sqrt{2} & 0 & 0 & 0 & 0 \\
\Omega/\sqrt{2} & \Delta_p & g & \Omega & 0 & 0 \\
0 & g & \Delta_r & 0 & \Omega/\sqrt{2} & 0 \\
0 & \Omega & 0 & \Delta_p + \Delta_c & \sqrt{2}g & 0 \\
0 & 0 & \Omega/\sqrt{2} & \sqrt{2}g & \Delta_p + \Delta_r & \sqrt{2}g \\
0 & 0 & 0 & 0 & \sqrt{2}g & 2\Delta_r
\end{bmatrix}, \quad (6)
$$

in which $\Omega = \chi_0/2$, and χ_0 is defined from $-\Phi_q \Phi_{\text{rf}}(t)/L_q = \chi(t)(a_q^\dagger + a_q)/\sqrt{2}$ and $\chi(t) = \chi_0 \cos(\omega t)$. Equation (6) indicates that in addition to the state-to-state interactions given in Eq. (5) and Fig. 2, the microwave further introduces couplings between the $|00\rangle$ and $|10\rangle$, $|10\rangle$ and $|20\rangle$, and $|01\rangle$ and $|11\rangle$ states with coupling strengths proportional to Ω.

The Lindblad master equation has the usual form:

$$
\dot{\rho} = -i[H^{\text{RWA}},\rho] + \sum_l \mathcal{D}[A_l]\rho, \quad (7)
$$

where ρ is the density matrix of the coupled qutrit-resonator system and $\mathcal{D}[A_l]\rho$ is the Lindblad operators containing various relaxation and dephasing processes:

$$
\mathcal{D}[A_l]\rho = (2A_l\rho A_l^\dagger - A_l^\dagger A_l\rho - \rho A_l^\dagger A_l)/2. \quad (8)
$$

The operators A_l can generally be written as $A_{ij} = \sqrt{\gamma_{ij}}|j\rangle\langle i|$, $A_{\varphi i} = \sqrt{2\gamma_{\varphi i}}|i\rangle\langle i|$, and $A_\kappa = \sqrt{\kappa}a_r$ for the qutrit energy relaxation, dephasing, and photon decay in the resonator, respectively. Here γ_{ij} denotes the relaxation rate from qutrit level i to level j and $\gamma_{\varphi i}$ is the dephasing rate of qutrit level i. Explicit expressions for these operators can be found in Appendix B.

III. EXPERIMENT

In the present work, we used an Al-junction-based rf-SQUID type phase qudit [34,35] which was coupled to a coplanar waveguide (CPW) resonator, as is shown schematically in Fig. 1. The qudit was described by three parameters: the junction's critical current I_c and capacitance C_q, and the SQUID loop inductance L_q. The CPW resonator had the effective parameters of capacitance C_r and inductance L_r, with a coupling capacitor C_c connecting to the qudit. The flux bias provided both dc and rf components of $\Phi_{\text{ext}} = \Phi_{\text{dc}} + \Phi_{\text{rf}}(t)$ for tuning the qudit level spacings and performing the state manipulation, respectively. The three-junction dc-SQUID was used for the qudit state readout. The sample was mounted on an oxygen-free copper platform thermally anchored to the mixing chamber of an Oxford cryogen-free dilution refrigerator which was cooled to $T \approx 10$ mK. The qudit control and measurement circuit included various filtering, attenuation, and amplification, and a trilayer μ-metal shield was used outside the outer vacuum chamber of the refrigerator [36–38].

The resonator had a measured fundamental frequency of $f_r = \omega_r/2\pi = 6.205$ GHz, and the qudit-resonator coupling strength was $g/2\pi \sim 18$ MHz. In the experiment, we changed the flux bias such that the qudit level spacings vary in the

TABLE I. The measured relaxation, dephasing, and decay rates for the phase qutrit-resonator system at the flux bias of $\Phi_{\text{dc}} = 0.7053 \, \Phi_0$ [40,41].

Parameter	γ_{10} (s^{-1})	γ_{21} (s^{-1})	$\gamma_{\varphi 1}$ (s^{-1})	$\gamma_{\varphi 2}$ (s^{-1})	κ (s^{-1})
	2.8×10^6	5.1×10^6	8.1×10^6	16.2×10^6	3.5×10^5

vicinity of ω_r and its energy spectra from single- or multiphoton excitation were traced out under increasing microwave power. By fitting the theoretical results to the experimental data, the qudit parameters in Fig. 1(a) were adjusted around designed values [39] and found to be $I_c = 1.21 \, \mu$A, $C_q = 1280$ fF, $L_q = 814$ pH, while the resonator had the parameters $C_r = 809$ fF, $L_r = 808$ pH, and $C_c = 5.5$ fF considering $\omega_r = 1/\sqrt{L_r C_r}$ and $Z_0 = (\pi/2)\sqrt{L_r/C_r} = 50 \, \Omega$. The corresponding Josephson energy and charging energy of the phase device are $E_J \approx 601$ GHz and $E_C \approx 15$ MHz, respectively.

For the master equation simulation, we measured the relaxation and dephasing rates at a given flux bias $\Phi_{\text{dc}} = 0.7053 \, \Phi_0$ with level spacings of $f_{10} = \omega_{10}/2\pi = 5.555$ GHz and $f_{21} = \omega_{21}/2\pi = 5.393$ GHz, which were away from f_r. The measured energy relaxation times in this case were $T_{10} = 1/\gamma_{10} = 353$ ns and $T_{21} = 1/\gamma_{21} = 196$ ns, respectively, while the dephasing time determined from Ramsey interference experiment was $T_{\varphi 1} = 1/\gamma_{\varphi 1} = 124$ ns [40]. The time decay of the photon state in the resonator was also measured, which leads to a $T_r = 1/\kappa = 2.866 \, \mu$s. These relaxation and decay rates, which were used in the master equation simulations, are summarized in Table I [41].

IV. RESULTS AND DISCUSSIONS

To measure the energy spectrum of the coupled qudit-resonator system, we apply a continuous single-tone microwave, namely, a microwave pulse with duration much greater than T_1. For a given level of microwave power, the dc flux bias and the microwave frequency in the neighborhood of the resonator frequency f_r are varied while the populations at the qudit excited states are monitored. The magnitude of the readout pulse is chosen such that the population of all the excited states ($P_1 + P_2 + P_3$) except that of the ground state (P_0) is measured. Figures 3(a)–3(c) show the measured results at three different microwave power levels. In Fig. 3(a), with low microwave power, the familiar avoided crossing is seen, which results from the dressed states formed from $|0\rangle_r|1\rangle_q$ and $|1\rangle_r|0\rangle_q$ when the qudit level spacing ω_{10} is varied in the neighborhood of the resonator frequency ω_r (see Fig. 1 for the uncoupled state labeling). Here only the first excited states of the qudit and resonator are involved at low microwave power. As the microwave power is increased, it can be seen in Fig. 3(b) that more spectral lines appear, as indicated by the white arrows. These spectral lines should arise from certain dressed states formed by different higher-excited uncoupled qudit-resonator states. In this case, the avoided crossing is located at a different qudit flux bias compared to that in Fig. 3(a). As is shown in Fig. 3(c), still new spectral lines appear, pointed out again by the white arrows, when the microwave power is further increased.

A. Energy spectrum of the qudit-resonator system

To understand how each of the spectral lines in Figs. 3(a)–3(c) forms and their origins, we calculate the eigenenergy levels and eigenvectors by solving the eigenvalue equation of the coupled qudit-resonator system, in which the applied microwave field is first disregarded as mentioned above. In Figs. 3(d)–3(f), we show the calculated energy spectra (solid lines) using the Hamiltonian H_0 in Eq. (A10) and the qudit-resonator parameters discussed above. In Fig. 3(d), the peak position of the experimental spectral lines in Fig. 3(a) (pointed out by two downward arrows) are plotted as solid squares, which agree very well with the calculated results. As discussed above, these spectral lines are from the dressed states of the uncoupled $|0\rangle_r|1\rangle_q$ and $|1\rangle_r|0\rangle_q$ when the qudit level spacing ω_{10} varies in the neighborhood of the resonator frequency ω_r. The downward-arrow pointed experimental lines in Figs. 3(b) and 3(c) with increasing microwave powers are also plotted as symbols in Figs. 3(e) and 3(f), respectively. The two upward-arrow pointed lines in Figs. 3(b) and 3(c) are found to be a single spectrum appearing under different microwave powers and, from the comparison between the data and numerical calculation discussed below, should be grouped into one spectral line in Fig. 3(e) (middle spectrum represented by the symbols).

The solid lines in Figs. 3(e) and 3(f) are the calculated energy levels using H_0, but with the magnitudes divided by 2 and 3, respectively. We see that the experimental data are fitted very well by the respective calculated results, which indicates that the experimental spectral lines in Figs. 3(b) and 3(c) pointed out by the arrows result from two- and three-photon processes with increasing microwave powers, respectively.

From the previously determined system parameters we find that the calculated coefficient η in the anharmonic term in Eq. (2) is small compared to the harmonic term ω_q. At the flux bias of $\Phi_{\text{dc}} = 0.6810 \, \Phi_0$, for instance, we have the calculated $\eta/2\pi \approx 91.5$ MHz and $\omega_q/2\pi \approx 6.29$ GHz, which lead to the parameter $\alpha = \eta/\omega_q \sim 0.015$. The qudit-resonator coupling strength $g/2\pi$ is calculated to be 17.3 MHz, which is much smaller compared to both ω_q and ω_r. With these parameters, we find that the calculated spectra using the approximated Hamiltonian H_0' (as $\alpha \to 0$) given by Eq. (5), when plotted also in Fig. 3, are almost indistinguishable from the solid lines calculated using H_0 [slight difference only visible in some parts of the lines in Fig. 3(f)], which indicates a good approximation of H_0 by H_0' for the present qudit device with small anharmonicity.

The Hamiltonian H_0' in Eq. (5) provides a clear physical picture of the main interactions in the coupled qudit-resonator system. In Fig. 2, we show the energy-level diagram of the system with the interactions in the limit of $\alpha \to 0$. The levels are aligned in the single-, two-, and three-photon resonant cases of $\omega_{10} = \omega_r$, $\omega_{20} = 2\omega_r$, and $\omega_{30} = 3\omega_r$, where the qudit level spacings increase as the dc flux bias decreases toward $0.5 \, \Phi_0$. With this, the observed qudit-resonator spectral lines in Figs. 3(a)–3(c) can be explained with a good approximation as follows. In Fig. 3(d), the dressed spectral lines (solid lines) result from the interaction of the $|1\rangle_r|0\rangle_q$ (dashed line) and $|0\rangle_r|1\rangle_q$ (dotted line) bare states with the coupling strength of g/π as symbolized by a circle in the figure. Similarly, in Fig. 3(e), the dressed spectral lines (solid lines) resulting
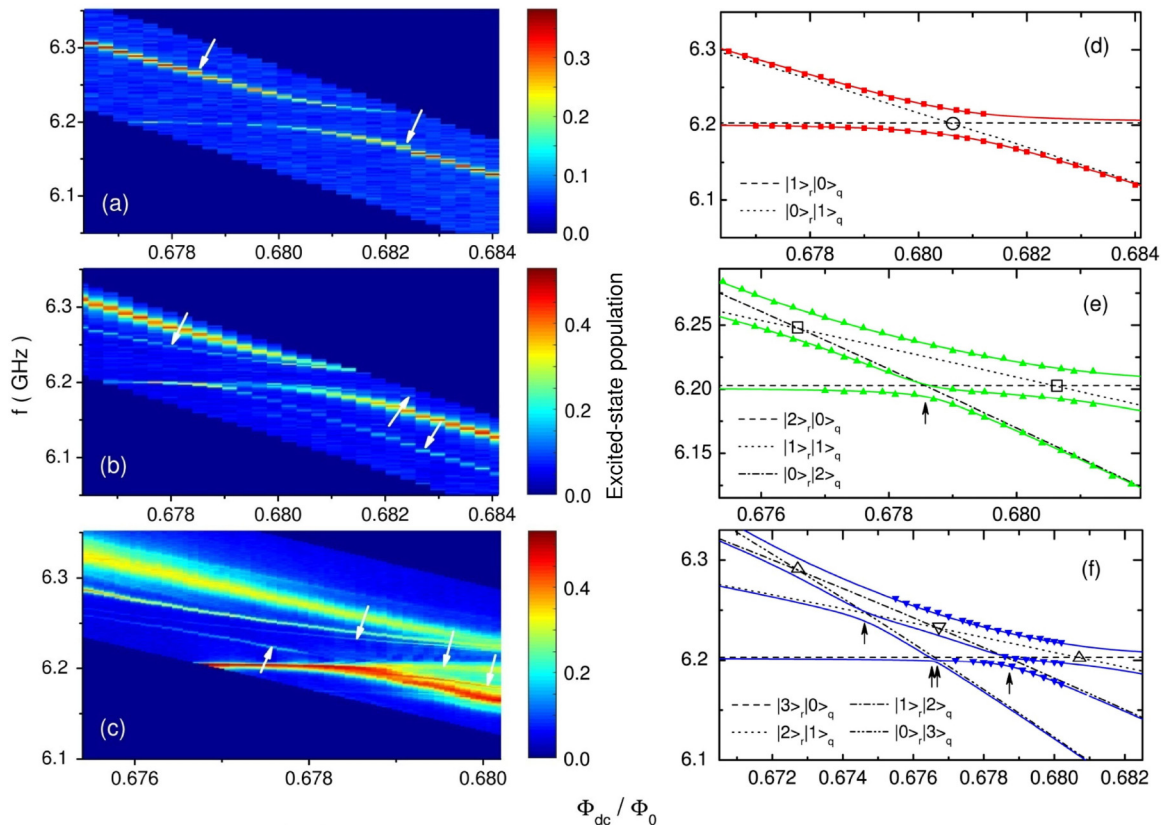
FIG. 3. Left panels: Experimental spectroscopic scans as a function of flux bias for three microwave driving powers. (a) -100 dBm; (b) -95 dBm; (c) -70 dBm. Right panels: Dressed state energy levels. Experimental (symbols) and theoretical (solid lines) spectral lines involving the first (d), the second (e), and the third (f) excited states of the qudit and resonator system shown in Fig. 2. Experimental data are taken from the spectra in (a)–(c) while the theoretical ones in (e) and (f) are the calculated results divided by a factor of 2 and 3, respectively. Note that the horizontal scales are different in (d), (e), and (f). The straight broken lines show the uncoupled qudit and resonator levels as indicated. The circle, squares, upward triangles, and downward triangle indicate the nearby bare state interaction strengths of g/π, $\sqrt{2}g/\pi$, $\sqrt{3}g/\pi$, and $2g/\pi$, respectively (see Fig. 2). Single and double arrows indicate weaker interactions between two states via one and two intermediate states, respectively.

from the interactions between the $|2\rangle_r|0\rangle_q$ (dashed line) and $|1\rangle_r|1\rangle_q$ (dotted line) bare states, and between the $|1\rangle_r|1\rangle_q$ (dotted line) and $|0\rangle_r|2\rangle_q$ (dashed-dotted line) bare states have the coupling strength of $\sqrt{2}g/\pi$ as indicated by two squares. A common feature of these results is that each bare states pair forming the dressed state splitting has direct interactions within the pair, namely, the states within the pair are linked by single-photon transitions, which can be seen clearly in Eq. (5) and Fig. 2.

The avoided crossing indicated by the arrow in Fig. 3(e) has a smaller splitting that seems to originate from the interaction between the $|2\rangle_r|0\rangle_q$ (dashed line) and $|0\rangle_r|2\rangle_q$ (dotted line) bare states. However, in addition to its small size, the splitting is different since there is no single-photon transition linking the two bare states. To further explain the result, we consider the 3×3 submatrix in Eq. (5) spanned in the $|02\rangle$, $|11\rangle$, $|20\rangle$ subspace (namely, in the 4th–6th rows and columns). If we look at the particular flux bias indicated by the arrow in Fig. 3(e), the three eigenvalues of the submatrix are found to be a and $(a + b \pm \delta)/2$, where $a = \epsilon_0 + E_2 = \epsilon_2 + E_0$, $b = \epsilon_1 + E_1$, and $\delta = \sqrt{(a - b)^2 + 16g^2}$. The corresponding eigenvectors are $[-1\ 0\ 1]$ and $[1\ (b - a \pm \delta)/2\sqrt{2}g\ 1]$ (unnormalized),

respectively. Hence one of the dressed state energies equals that of the $|0\rangle_r|2\rangle_q$ and $|2\rangle_r|0\rangle_q$ bare states at their degeneracy point, while the other two locate at the points shifted upward and downward, respectively, by an amount of $\delta/2$ from the average value of the bare state energies a and b. The normalized eigenvectors can be written explicitly as $[0.350\ 0.869\ 0.350]$, $[-0.707\ 0\ 0.707]$, and $[0.614\ -0.495\ 0.614]$ for the three dressed states with decreasing energies in Fig. 3(e). The dressed state with highest energy is therefore a superposition of three bare states $|0\rangle_r|2\rangle_q$, $|1\rangle_r|1\rangle_q$, and $|2\rangle_r|0\rangle_q$, with a prevailing contribution from the $|1\rangle_r|1\rangle_q$ state of 75.5%. While the middle dressed state is a superposition of the $|0\rangle_r|2\rangle_q$ and $|2\rangle_r|0\rangle_q$ states, the lowest one still has a 24.5% contribution from the $|1\rangle_r|1\rangle_q$ state, which is therefore involved in the small splitting seemingly originating from the $|2\rangle_r|0\rangle_q$ and $|0\rangle_r|2\rangle_q$ states due to the absence of single-photon linkage between them. As a comparison, the three dressed-state eigenvectors at the flux biases corresponding to the left and right avoided crossings indicated by the two squares in Fig. 3(e), arranged with decreasing energies, are $[0.662\ 0.734\ 0.152]$, $[-0.746\ 0.628\ 0.218]$, $[0.065\ -0.258\ 0.964]$ and $[0.661\ 0.734\ 0.154]$, $[0.747\ -0.626\ -0.223]$, $[0.067\ -0.263\ 0.963]$, respectively.
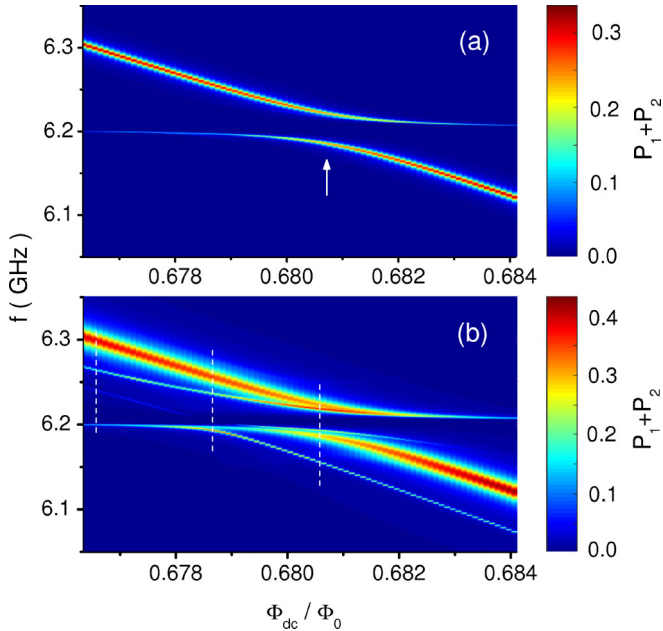
FIG. 4. Calculated spectra a function of flux bias at the microwave driving powers of (a) $\Omega/2\pi = 1.1$ MHz and (b) $\Omega/2\pi = 3.5$ MHz. The arrow in (a) indicates the resonant point. Three vertical dashed lines in (b) indicate the cuts at flux biases of $\Phi_{dc} = 0.6766$, 0.6786, and 0.6806 Φ_0, respectively.

So the dressed-state pair at the left (right) avoided crossing has an overwhelming contribution of >95% from their corresponding bare states of $|1\rangle_r|1\rangle_q$ and $|0\rangle_r|2\rangle_q$ ($|2\rangle_r|0\rangle_q$ and $|1\rangle_r|1\rangle_q$).

Similar explanations can also be made for the data in Fig. 3(f), in which four higher-excited bare states are involved and three single-photon linkages with two different strengths of $\sqrt{3}g/\pi$ and $2g/\pi$ (see Fig. 2) lead to the three splittings that are indicated by up and down triangles, respectively. Two smaller splittings, indicated by two single arrows, result approximately from interactions taking account of an additional third bare state, similar to the result discussed above for Fig. 3(e). In Fig. 3(f), the smallest splitting indicated by the double arrows originates from the interactions where a fourth bare state needs to be considered.

B. Master equation solutions

In order to have a better understanding of the level population distribution and the intensity of the experimental spectral lines in Figs. 3(a)–3(c), we take into account the microwave field applied in the measurement as well as various relaxation, dephasing, and decay processes, considering the simpler qutrit-resonator system as an example. Such a dynamical system can be described in terms of the Lindblad master equation, from which it is possible to discuss the contributions from different energy-level populations to the spectral lines shown in Figs. 3(a)–3(c) (note that all the excited-states populations are measured in the experimental data).

In Fig. 4 we show the calculated qutrit excited-states population $P_1 + P_2$ using the relaxation, dephasing, and decay parameters listed in Table I. It can be seen that the results
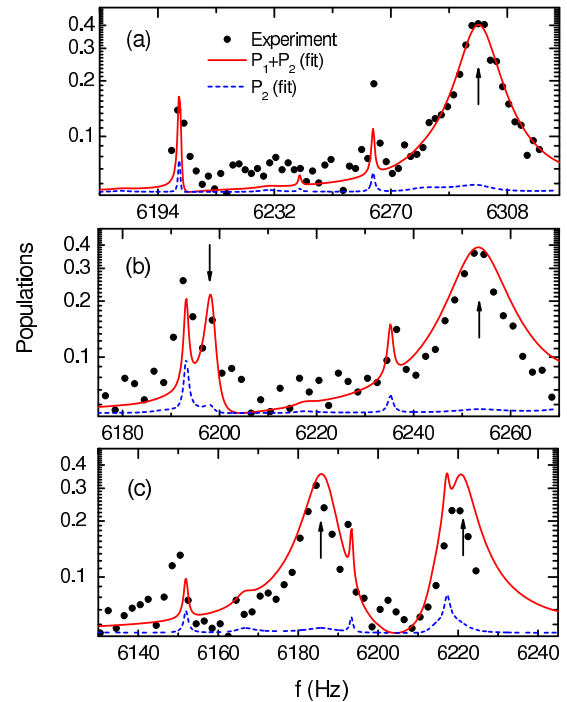

FIG. 5. Calculated spectra at the microwave driving powers of $\Omega/2\pi = 3.5$ MHz (lines). (a) $\Phi_{dc} = 0.6766\,\Phi_0$, (b) $\Phi_{dc} = 0.6786\Phi_0$, and (c) $\Phi_{dc} = 0.6806\Phi_0$, corresponding to the three cuts in Fig. 4(b). Symbols are the experimental data measured at microwave power of -95 dBm.

in Fig. 4(a) reproduce very well the experimental data in Fig. 3(a). With a similar factor of the microwave power increase, the numerical results in Fig. 4(b) also reproduce those in Fig. 3(b), indicating a good agreement between the theory and experiment. A slight difference in the latter case is that the experimental spectral line at a higher microwave power level shown in Fig. 3(c) and pointed out by an upward arrow starts to appear (though not clearly) in the calculated spectra in Fig. 4(b) at the lower microwave power level.

The result in Fig. 4(a) is calculated at a low microwave power level where single-photon excitation is involved. In this case, the population P_2 at the second-excited state is approximately zero and for the data at the center of avoided crossing, as pointed out by an arrow, the dressed states are the equal superpositions of the bare states $|1\rangle_r|0\rangle_q$ and $|0\rangle_r|1\rangle_q$. The spectral line is therefore composed of two peaks with equal height and width. Away from the avoided crossing, the height and width of the two peaks will change in opposite directions, with one peak evolving to the $|1\rangle_r|0\rangle_q$ state showing decreasing qutrit population P_1 while the other to the $|0\rangle_r|1\rangle_q$ state showing increasing P_1 [see Fig. 3(d)]. These are confirmed by the master equation simulations, from which it is also seen that the process as well as the line shapes is influenced by the coherence times of the coupled qutrit-resonator system.

The solid lines in Fig. 5 from (a) to (c) are the data in Fig. 4(b) along the three cuts indicated by the vertical dashed lines from left to right, respectively, while symbols are the corresponding experimental results in Fig. 3(b). The dashed lines are the calculated second-excited-state population P_2. The three cuts correspond to the positions of the three avoided

crossings denoted by the left square, the arrow, and the right square in Fig. 3(e). At this higher microwave power level, we see that P_2 has significant contributions at certain frequencies resulting from the two-photon excitation. The spectral peaks from the single-photon excitation discussed above become higher and broader under higher microwave power driving. These peaks, as indicated by upward arrows in Fig. 5, still have predominant P_1 (also P_0; note that $P_0 + P_1 + P_2 = 1$) contributions, with the ratio $P_2/(P_1 + P_2)$ below 0.03. Other peaks are contributed by P_1, P_2, and also P_0 of the dressed states formed by the bare states $|2\rangle_r|0\rangle_q$, $|1\rangle_r|1\rangle_q$, and $|0\rangle_r|2\rangle_q$ as shown in Fig. 3(e). We point out that when the system's coherence times increase, the spectral peaks will become sharper, namely, their height and width will increase and decrease, respectively.

C. Applications

There are a number of studies in which the coupled qutrit-resonator or qudit-resonator systems are involved [24–29,33]. Our results can provide better understanding and control of the experiments. For instance, the creation of N-photon NOON states was studied in a coupled qutrit-resonator system [29]. In this experiment, two qutrits q_1 and q_2 are both coupled to a bus resonator C while they are individually coupled to the storage resonators A and B, respectively. The NOON states in A and B with N up to 3 are experimentally demonstrated. We show that the preparation of such states can be visualized and better controlled with the help of our results such as those shown in Figs. 2 and 3.

The NOON state preparation with arbitrary N starts by exciting q_1 to its first excited state, which is then half-swapped to C by bringing them into resonance. This process follows basically a route in Fig. 2 from $|00\rangle$ to $|01\rangle$ (excitation, off resonance) and then to $|10\rangle$ (swap, on resonance), with the swap being performed at the point indicated by the circle in Fig. 3(d). After this, q_1 is set off resonance while q_2 is brought to resonance with C and the state in C is fully swapped to q_2, thus generating a Bell state in the coupled q_1 and q_2. Then, for the $N = 3$ NOON state, each qutrit goes through a route from $|01\rangle$ to $|02\rangle$ (excitation, off resonance) to $|11\rangle$ (swap, on resonance) to $|12\rangle$ (excitation, off resonance) to $|21\rangle$ (swap, on resonance) in Fig. 2, with the two swaps performed at the points indicated by the left square in Fig. 3(e) and down triangle in Fig. 3(f), respectively. Finally both qutrits follow the route from $|21\rangle$ to $|30\rangle$ in Fig. 2 by swapping at the point indicated by the right up triangle in Fig. 3(f), thus creating the $N = 3$ NOON state. In this experiment, suitable qutrits bias points can be easily known from Figs. 3(d)–3(f) and state coupling strength from Fig. 2, which is critical for determining the swap time.

The coupled qubit-resonator system is often used for the quantum state measurement [6–8]. Very recent works have found that such measurements can induce state transitions out of the two-level subspace of the qubit if the measurement microwave power (or the number of photons) in the resonator is increased to a high level [33]. The excitation to the fifth-excited states was observed and explained using the Jaynes-Cummings model with terms usually ignored in the rotating-wave approximation. Within our theoretical framework, a reverse process can readily be considered: What will be the
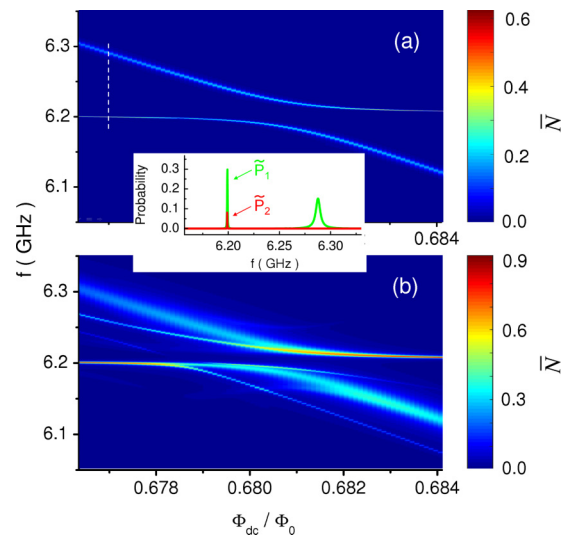

FIG. 6. Calculated average photon number $\overline{N}$ in the resonator versus qudit flux bias and microwave frequency at the microwave powers of (a) $\Omega/2\pi = 1.1$ MHz and (b) $\Omega/2\pi = 3.5$ MHz, corresponding to those in Fig. 4. Inset shows the probabilities $\tilde{P}_1$ and $\tilde{P}_2$ with one and two photons in the resonator along the dashed line in (a). Note that $\overline{N} = \tilde{P}_1 + 2\tilde{P}_2$ (see Appendix B).

photon number in the resonator when the qutrit or qudit is driven with increasingly higher microwave power? In Fig. 6, we show the calculated results of the average photon number $\overline{N}$ in the resonator (see Appendix B) versus qudit flux bias and microwave frequency at two microwave powers of $\Omega/2\pi = $ 1.1 and 3.5 MHz, which correspond to the power levels in Fig. 4. In the case of Fig. 6(a), it can be seen that although the microwave is applied directly to the qudit only, there will be considerable excitation of photons in the resonator when the microwave frequency is near the frequencies of both the resonator (ω_r) and qudit (ω_{10}).

This may not be surprising since the qudit and resonator form a coupled system. In the inset of Fig. 6, we show the probabilities $\tilde{P}_1$ and $\tilde{P}_2$ of having one and two photons in the resonator at a flux bias of $\Phi_{\mathrm{dc}} = 0.6770\Phi_0$ [along the dashed line in Fig. 6(a)]. Note that $\overline{N} = \tilde{P}_1 + 2\tilde{P}_2$. $\tilde{P}_1$ shows two peaks near ω_r and ω_{10} while $\tilde{P}_2$ has one peak near ω_r. In Fig. 6(b), more photon spectral lines can be seen as the microwave power increases. In this case, more qudit energy levels and multiphoton processes are involved.

V. SUMMARY

We systematically studied the energy spectrum of the coupled superconducting phase qudit-resonator system where the qudit level spacings were varied around the resonator frequency by changing the applied magnetic flux bias. The experimental spectra were measured with increasing microwave power so that the emergence of multiphoton processes were clearly observed and populations up to the third-excited level of the qudit were detected. Using the experimentally determined sample parameters, the calculated spectra of the qudit-resonator system fitted the experimental data very well. In particular, due to the small anharmonicity of the phase device a simplified theoretical model capturing the leading-order

qudit-resonator interactions was proposed to account for the experimental results. The Lindblad master equation was also used to calculate the level populations for the case of the qutrit-resonator system, which provided a detailed description of the dynamics of the system under the microwave excitation. These results are useful to understand and perform experiments in coupled multilevel-resonator systems, and are also applicable to artificial atoms with weak anharmonicity such as the transmon and Xmon devices.

APPENDIX A: THE EIGENVALUE PROBLEM OF THE QUDIT-RESONATOR SYSTEM

The Hamiltonian of the coupled qudit-resonator system (see Fig. 1 for various parameters and symbols) can be written as

$$H = H_q + H_r + H_c \tag{A1}$$

with the subscripts q, r, and c denoting the qudit, the resonator, and their coupling, respectively:

$$
\begin{aligned}
H_q &= \frac{1}{2}\frac{Q_q^2}{C_q'} + \frac{(\Phi_q - \Phi_{\text{ext}})^2}{2L_q} - E_J \cos\left(2\pi\frac{\Phi_q}{\Phi_0}\right) \\
&\approx \frac{1}{2}\frac{Q_q^2}{C_q'} + \frac{(\Phi_q - \Phi_{\text{dc}})^2}{2L_q} - E_J \cos\left(2\pi\frac{\Phi_q}{\Phi_0}\right) - \frac{\Phi_q \Phi_{\text{rf}}(t)}{L_q} \\
&\equiv H_q^0 - \frac{\Phi_q \Phi_{\text{rf}}(t)}{L_q},
\end{aligned}
\tag{A2}
$$

$$H_r = \frac{1}{2}\frac{Q_r^2}{C_r'} + \frac{\Phi_r^2}{2L_r}, \tag{A3}$$

$$H_c = \frac{Q_q Q_r}{C_c'}, \tag{A4}$$

in which Φ_0 is the flux quantum, $E_J = (\Phi_0/2\pi)I_c$, $\Phi_{\text{rf}}(t) = A\cos(\omega t)$ represents the applied microwave field with ω being the microwave frequency, and $\Phi_{q,r}$ and $Q_{q,r}$ are the canonically conjugate variables. In particular, they represent the flux and charge in the case of the qudit. C_q', C_r', and C_c' are defined by

$$
\begin{aligned}
C_q' &= (C_r C_c + C_c C_q + C_q C_r)/(C_r + C_c), \\
C_r' &= (C_r C_c + C_c C_q + C_q C_r)/(C_q + C_c), \\
C_c' &= (C_r C_c + C_c C_q + C_q C_r)/C_c.
\end{aligned}
$$

It can be seen that as $C_c \to 0$, we have $C_q' \to C_q$, $C_r' \to C_r$, and $C_c' \to C_q C_r/C_c$. Now we consider the time-independent part of the Hamiltonian:

$$H_0 = H_q^0 + H_r + H_c. \tag{A5}$$

Expanding the qudit potential as Taylor series around the local minimum, H_q^0 in Eq. (A2) can be written as [15]

$$H_q^0 = \frac{1}{2}\frac{Q_q^2}{C_q'} + \frac{\Phi_q^2}{2L_J^*} + \frac{\Phi_q^3}{2\Phi_0 L^*} \tag{A6}$$

where

$$
\begin{aligned}
L_J^* &= L_J/\lambda, \\
L^* &= 3L_q/\pi(2\lambda + \xi), \\
\lambda &= [2 + \pi(1 - 4\Phi_{\text{dc}}/\Phi_0)\beta^{-1} + \beta^{-2}]^{1/2}, \\
\xi &= 4\pi\Phi_{\text{dc}}/\Phi_0 - 2\beta^{-1} - \pi,
\end{aligned}
$$

with $L_J = \Phi_0/(2\pi I_c)$ and $\beta = (2\pi L_q I_c)/\Phi_0$. Introducing the creation and annihilation operators $a_q^\dagger$ and a_q for the harmonic part of Eq. (A6), defined by

$$\Phi_q = \sqrt{\frac{1}{2C_q'\omega_q}}(a_q^\dagger + a_q), \quad Q_q = \sqrt{\frac{C_q'\omega_q}{2}}(a_q^\dagger - a_q),$$

where $\omega_q = \sqrt{1/L_J^* C_q'}$ is the Josephson plasma frequency, we can write the Hamiltonian of the qudit as

$$H_q^0 = \omega_q\left(a_q^\dagger a_q + \tfrac{1}{2}\right) + \eta(a_q^\dagger + a_q)^3, \tag{A7}$$

where $\eta = (1/2C_q'\omega_q)^{3/2}/2\Phi_0 L^*$. The qudit Hamiltonian H_q^0 in Eq. (A7) can be diagonalized, which leads to the bottom four eigenvalues of $E_0 = \omega_q/2 - 11\eta^2/\omega_q$, $E_1 = 3\omega_q/2 - 71\eta^2/\omega_q$, $E_2 = 5\omega_q/2 - 191\eta^2/\omega_q$, and $E_3 = 7\omega_q/2 - 371\eta^2/\omega_q$.

In a similar way, using the creation and annihilation operators:

$$\Phi_r = \sqrt{\frac{1}{2C_r'\omega_r}}(a_r^\dagger + a_r), \quad Q_r = \sqrt{\frac{C_r'\omega_r}{2}}(a_r^\dagger - a_r),$$

the Hamiltonian of the resonator can be written as

$$H_r = \omega_r\left(a_r^\dagger a_r + \tfrac{1}{2}\right), \tag{A8}$$

where $\omega_r = \sqrt{1/L_r C_r'}$. Finally the interaction Hamiltonian reads

$$H_c = g(a_q^\dagger a_r + a_r^\dagger a_q), \tag{A9}$$

where $g = \sqrt{\omega_q C_q'/2}\sqrt{\omega_r C_r'/2}/C_c'$ is the coupling strength. In the present experiment the measured energy spectra of the coupled system show the spectral lines of the dressed states resulting from up to the third-excited states of both the qudit and resonator components. To explain these results we write the time-independent Hamiltonian H_0 in the matrix form in the subspace $\{|00\rangle, |01\rangle, |10\rangle, |02\rangle, |11\rangle, |20\rangle, |03\rangle, |12\rangle, |21\rangle, |30\rangle\}$, with the two indices in each base vector denoted for the eigenstates of H_r and H_q^0, respectively:

$$H_0 = \begin{bmatrix} \epsilon_0 + E_0 & 0 & -3\alpha g & 0 & 3\alpha^2 g & 0 & 0 & -\sqrt{2}\alpha & 0 & 0 \\ 0 & \epsilon_0 + E_1 & \left(1 + \frac{116}{3}\alpha^2\right)g & 0 & -9\alpha g & 0 & 0 & -36\sqrt{2}\alpha^2 g & 0 & 0 \\ -3\alpha g & \left(1 + \frac{116}{3}\alpha^2\right)g & \epsilon_1 + E_0 & 3\sqrt{2}\alpha g & 0 & -3\sqrt{2}\alpha g & -11\sqrt{6}\alpha^2 g & 0 & 3\sqrt{2}\alpha^2 g & 0 \\ 0 & 0 & 3\sqrt{2}\alpha g & \epsilon_0 + E_2 & \left(\sqrt{2} + \frac{560}{3}\sqrt{2}\alpha^2\right)g & 0 & 0 & -15\alpha g & 0 & 0 \\ 3\alpha^2 g & -9\alpha g & 0 & \left(\sqrt{2} + \frac{560}{3}\sqrt{2}\alpha^2\right)g & \epsilon_1 + E_1 & \left(\sqrt{2} + \frac{116}{3}\sqrt{2}\alpha^2\right)g & 3\sqrt{6}\alpha g & 0 & -9\sqrt{2}\alpha g & 0 \\ 0 & 0 & -3\sqrt{2}\alpha g & 0 & \left(\sqrt{2} + \frac{116}{3}\sqrt{2}\alpha^2\right)g & \epsilon_2 + E_0 & 0 & 3\sqrt{2}\alpha g & 0 & -3\sqrt{3}\alpha g \\ 0 & 0 & -11\sqrt{6}\alpha^2 g & 0 & 3\sqrt{6}\alpha g & 0 & \epsilon_0 + E_3 & \left(\sqrt{3} + \frac{1660}{3}\alpha^2\right)g & 0 & 0 \\ -\sqrt{2}\alpha g & -36\sqrt{2}\alpha^2 g & 0 & -15\alpha g & 0 & 3\sqrt{2}\alpha g & \left(\sqrt{3} + \frac{1660}{3}\alpha^2\right)g & \epsilon_1 + E_2 & \left(2 + \frac{1120}{3}\alpha^2\right)g & 0 \\ 0 & 0 & 3\sqrt{2}\alpha^2 g & 0 & -9\sqrt{2}\alpha g & 0 & 0 & \left(2 + \frac{1120}{3}\alpha^2\right)g & \epsilon_2 + E_1 & \left(\sqrt{3} + \frac{116}{3}\sqrt{3}\alpha^2\right)g \\ 0 & 0 & 0 & 0 & 0 & -3\sqrt{3}\alpha g & 0 & 0 & \left(\sqrt{3} + \frac{116}{3}\sqrt{3}\alpha^2\right)g & \epsilon_3 + E_0 \end{bmatrix}, \tag{A10}$$

where $\epsilon_n = \omega_r(n + 1/2)$ and $\alpha = \eta/\omega_q$. The eigenvalues of the coupled qudit-resonator system can be obtained by solving Eq. (A10).

APPENDIX B: THE LINDBLAD MASTER EQUATION

The Lindblad master equation has the form

$$\dot{\rho} = -i[H,\rho] + \sum_l \mathcal{D}[A_l]\rho, \tag{B1}$$

where ρ is the density matrix of the coupled qutrit-resonator system, H is the total Hamiltonian including the time-dependent driving microwave term,

$$H = H_0 - \Phi_q \Phi_{\mathrm{rf}}(t)/L_q, \tag{B2}$$

and $\mathcal{D}[A_l]\rho$ is the Lindblad operators containing various relaxation and dephasing processes:

$$\mathcal{D}[A_l]\rho = (2A_l\rho A_l^\dagger - A_l^\dagger A_l\rho - \rho A_l^\dagger A_l)/2. \tag{B3}$$

The second term on the right-hand side of Eq. (B2) can be written as $-\Phi_q \Phi_{\mathrm{rf}}(t)/L_q = \chi(t)(a_q^\dagger + a_q)/\sqrt{2}$ with

$$\chi(t) = -\frac{\Phi_{\mathrm{rf}}(t)}{L}\sqrt{\frac{1}{C_q'\omega_q}} = \chi_0\cos(\omega t). \tag{B4}$$

To discuss the qutrit we restrict ourselves in the subspace $\{|00\rangle, |01\rangle, |10\rangle, |02\rangle, |11\rangle, |20\rangle\}$ and replace H_0 with H_0' given in Eq. (5) so the Hamiltonian H becomes $H' = H_0' - \Phi_q \Phi_{\mathrm{rf}}(t)/L_q$, which is expressed in the 6×6 matrix form:

$$H' = \begin{bmatrix} 0 & \chi/\sqrt{2} & 0 & 0 & 0 & 0 \\ \chi/\sqrt{2} & \omega_{10} & g & \chi & 0 & 0 \\ 0 & g & \omega_r & 0 & \chi/\sqrt{2} & 0 \\ 0 & \chi & 0 & \omega_{10}+\omega_{21} & \sqrt{2}g & 0 \\ 0 & 0 & \chi/\sqrt{2} & \sqrt{2}g & \omega_r+\omega_{10} & \sqrt{2}g \\ 0 & 0 & 0 & 0 & \sqrt{2}g & 2\omega_r \end{bmatrix}, \tag{B5}$$

in which $\omega_{10} = E_1 - E_0$ and $\omega_{21} = E_2 - E_1$. If we perform a unitary transformation

$$H'' = U^\dagger H' U - i(\partial U^\dagger/\partial t)U \tag{B6}$$

with

$$U = \begin{bmatrix} 1 & 0 & 0 & 0 & 0 & 0 \\ 0 & e^{-i\omega t} & 0 & 0 & 0 & 0 \\ 0 & 0 & e^{-i\omega t} & 0 & 0 & 0 \\ 0 & 0 & 0 & e^{-i2\omega t} & 0 & 0 \\ 0 & 0 & 0 & 0 & e^{-i2\omega t} & 0 \\ 0 & 0 & 0 & 0 & 0 & e^{-i2\omega t} \end{bmatrix}, \tag{B7}$$

which brings the system to a doubly rotating reference frame with frequencies of ω and 2ω, we have

$$H'' = \begin{bmatrix} 0 & (1+e^{i2\omega t})\chi_0/2\sqrt{2} & 0 & 0 & 0 & 0 \\ (e^{-i2\omega t}+1)\chi_0/2\sqrt{2} & \omega_{10}-\omega & g & (1+e^{i2\omega t})\chi_0/2 & 0 & 0 \\ 0 & g & \omega_r-\omega & 0 & (1+e^{i2\omega t})\chi_0/2\sqrt{2} & 0 \\ 0 & (e^{-i2\omega t}+1)\chi_0/2 & 0 & (\omega_{10}+\omega_{21})-2\omega & \sqrt{2}g & 0 \\ 0 & 0 & (e^{-i2\omega t}+1)\chi_0/2\sqrt{2} & \sqrt{2}g & (\omega_r+\omega_{10})-2\omega & \sqrt{2}g \\ 0 & 0 & 0 & 0 & \sqrt{2}g & 2\omega_r-2\omega \end{bmatrix}. \tag{B8}$$

Furthermore, if we define $\Delta_p = \omega_{10} - \omega$, $\Delta_c = \omega_{21} - \omega$, $\Delta_r = \omega_r - \omega$, and perform a rotating-wave approximation to drop terms oscillating with frequency 2ω, we arrive at

$$
H^{\mathrm{RWA}} = \begin{bmatrix}
0 & \Omega/\sqrt{2} & 0 & 0 & 0 & 0 \\
\Omega/\sqrt{2} & \Delta_p & g & \Omega & 0 & 0 \\
0 & g & \Delta_r & 0 & \Omega/\sqrt{2} & 0 \\
0 & \Omega & 0 & \Delta_p + \Delta_c & \sqrt{2}g & 0 \\
0 & 0 & \Omega/\sqrt{2} & \sqrt{2}g & \Delta_p + \Delta_r & \sqrt{2}g \\
0 & 0 & 0 & 0 & \sqrt{2}g & 2\Delta_r
\end{bmatrix}
\tag{B9}
$$

in which $\Omega = \chi_0/2$.

The operators A_l in Eq. (B3) can generally be written as $A_{ij} = \sqrt{\gamma_{ij}}|j\rangle\langle i|$, $A_{\varphi i} = \sqrt{2\gamma_{\varphi i}}|i\rangle\langle i|$, and $A_\kappa = \sqrt{\kappa}\,a_r$ for the qutrit energy relaxation, dephasing, and photon decay in the resonator, respectively. Here γ_{ij} denotes the relaxation rate from qutrit level i to level j and $\gamma_{\varphi i}$ is the dephasing rate of qutrit level i. These parameters are all related to the experimentally measurable ones through $\gamma_{10} = 1/T_{10}$, $\gamma_{21} = 1/T_{21}$, $\gamma_{\varphi 1} = 1/T_{\varphi 1}$, $\gamma_{\varphi 2} = 1/T_{\varphi 2}$, $\kappa = 1/T_r$. The operators A_l for these processes can therefore be written in the matrix form as

$$
A_{10} = \sqrt{\gamma_{10}} \begin{bmatrix}
0 & 1 & 0 & 0 & 0 & 0 \\
0 & 0 & 0 & 0 & 0 & 0 \\
0 & 0 & 0 & 0 & 1 & 0 \\
0 & 0 & 0 & 0 & 0 & 0 \\
0 & 0 & 0 & 0 & 0 & 0 \\
0 & 0 & 0 & 0 & 0 & 0
\end{bmatrix},
\tag{B10}
$$

$$
A_{21} = \sqrt{\gamma_{21}} \begin{bmatrix}
0 & 0 & 0 & 0 & 0 & 0 \\
0 & 0 & 0 & 1 & 0 & 0 \\
0 & 0 & 0 & 0 & 0 & 0 \\
0 & 0 & 0 & 0 & 0 & 0 \\
0 & 0 & 0 & 0 & 0 & 0 \\
0 & 0 & 0 & 0 & 0 & 0
\end{bmatrix},
\tag{B11}
$$

$$
A_{\varphi_1} = \sqrt{\gamma_{\varphi_1}} \begin{bmatrix}
0 & 0 & 0 & 0 & 0 & 0 \\
0 & 1 & 0 & 0 & 0 & 0 \\
0 & 0 & 0 & 0 & 0 & 0 \\
0 & 0 & 0 & 0 & 0 & 0 \\
0 & 0 & 0 & 0 & 1 & 0 \\
0 & 0 & 0 & 0 & 0 & 0
\end{bmatrix},
\tag{B12}
$$

$$
A_{\varphi_2} = \sqrt{\gamma_{\varphi_2}} \begin{bmatrix}
0 & 0 & 0 & 0 & 0 & 0 \\
0 & 0 & 0 & 0 & 0 & 0 \\
0 & 0 & 0 & 0 & 0 & 0 \\
0 & 0 & 0 & 1 & 0 & 0 \\
0 & 0 & 0 & 0 & 0 & 0 \\
0 & 0 & 0 & 0 & 0 & 0
\end{bmatrix},
\tag{B13}
$$

$$
A_\kappa = \sqrt{\kappa} \begin{bmatrix}
0 & 0 & 1 & 0 & 0 & 0 \\
0 & 0 & 0 & 0 & 1 & 0 \\
0 & 0 & 0 & 0 & 0 & \sqrt{2} \\
0 & 0 & 0 & 0 & 0 & 0 \\
0 & 0 & 0 & 0 & 0 & 0 \\
0 & 0 & 0 & 0 & 0 & 0
\end{bmatrix}.
\tag{B14}
$$

We note that in Eq. (B10) there are two nonzero matrix elements, which correspond to the cases when the resonator is in the zero- or one-photon state. In Eq. (B11) the second nonzero element corresponding to the one-photon state of the resonator does not appear due to the smaller subspace we have considered. A similar situation occurs for Eqs. (B12) and (B13), respectively.

In the same subspace $\{|00\rangle, |01\rangle, |10\rangle, |02\rangle, |11\rangle, |20\rangle\}$, the density matrix can be written as

$$\rho = \begin{bmatrix} \rho_{00} & \rho_{01} & \rho_{02} & \rho_{03} & \rho_{04} & \rho_{05} \\ \rho_{10} & \rho_{11} & \rho_{12} & \rho_{13} & \rho_{14} & \rho_{15} \\ \rho_{20} & \rho_{21} & \rho_{22} & \rho_{23} & \rho_{24} & \rho_{25} \\ \rho_{30} & \rho_{31} & \rho_{32} & \rho_{33} & \rho_{34} & \rho_{35} \\ \rho_{40} & \rho_{41} & \rho_{42} & \rho_{43} & \rho_{44} & \rho_{45} \\ \rho_{50} & \rho_{51} & \rho_{52} & \rho_{53} & \rho_{54} & \rho_{55} \end{bmatrix}. \tag{B15}$$

Using Eqs. (B9)–(B15), one is able to find the steady-state solution of ρ from Eq. (B1). The qutrit level populations are finally given by

$$P_0 = \rho_{00} + \rho_{22} + \rho_{55},$$
$$P_1 = \rho_{11} + \rho_{44}, \tag{B16}$$
$$P_2 = \rho_{33}.$$

Since the probabilities of having one and two photons in the resonator are $\tilde{P}_1 = \rho_{22} + \rho_{44}$ and $\tilde{P}_2 = \rho_{55}$, respectively, the average number of photons in the resonator is

$$\overline{N} = \rho_{22} + \rho_{44} + 2\rho_{55}, \tag{B17}$$

or

$$\overline{N} = \tilde{P}_1 + 2\tilde{P}_2. \tag{B18}$$

[1] J. Clarke and F. K. Wilhelm, Nature (London) **453**, 1031 (2008).

[2] M. H. Devoret and R. J. Schoelkopf, Science **339**, 1169 (2013).

[3] C.-P. Yang, S.-I. Chu, and S. Han, Phys. Rev. A **67**, 042311 (2003).

[4] J. Q. You and F. Nori, Phys. Rev. B **68**, 064509 (2003).

[5] I. M. Georgescu, S. Ashhab, and F. Nori, Rev. Mod. Phys. **86**, 153 (2014).

[6] A. Blais, R.-S. Huang, A. Wallraff, S. M. Girvin, and R. J. Schoelkopf, Phys. Rev. A **69**, 062320 (2004).

[7] J. Gambetta, A. Blais, D. I. Schuster, A. Wallraff, L. Frunzio, J. Majer, M. H. Devoret, S. M. Girvin, and R. J. Schoelkopf, Phys. Rev. A **74**, 042318 (2006).

[8] M. D. Reed, L. DiCarlo, B. R. Johnson, L. Sun, D. I. Schuster, L. Frunzio, and R. J. Schoelkopf, Phys. Rev. Lett. **105**, 173601 (2010).

[9] O Viehmann, J. von Delft, and F. Marquardt, Phys. Rev. Lett. **110**, 030601 (2013).

[10] A. Kurcz, A. Bermudez, and J. J. García-Ripoll, Phys. Rev. Lett. **112**, 180405 (2014).

[11] F. Mei, V. M. Stojanović, I. Siddiqi, and L. Tian, Phys. Rev. B **88**, 224502 (2013).

[12] K. Seo and L. Tian, Phys. Rev. B **91**, 195439 (2015).

[13] J. Q. You and F. Nori, Nature (London) **474**, 589 (2011).

[14] M. A. Sillanpää, J. Li, K. Cicak, F. Altomare, J. I. Park, R. W. Simmonds, G. S. Paraoanu, and P. J. Hakonen, Phys. Rev. Lett. **103**, 193601 (2009).

[15] J. Li, G. S. Paraoanu, K. Cicak, F. Altomare, J. I. Park, R. W. Simmonds, M. A. Sillanpää, and P. J. Hakonen, Phys. Rev. B **84**, 104527 (2011).

[16] J. Li, G. S. Paraoanu, K. Cicak, F. Altomare, J I. Park, R. W. Simmonds, M. A. Sillanpää, and P. J. Hakonen, Sci. Rep. **2**, 645 (2012).

[17] A. A. Abdumalikov, Jr., O. Astafiev, A. M. Zagoskin, Yu. A. Pashkin, Y. Nakamura, and J. S. Tsai, Phys. Rev. Lett. **104**, 193601 (2010).

[18] S. Novikov, J. E. Robinson, Z. K. Keane, B. Suri, F. C. Wellstood, and B. S. Palmer, Phys. Rev. B **88**, 060503 (2013).

[19] K. S. Kumar, A. Vepsäläinen, S. Danilin, and G. S. Paraoanu, Nat. Commun. **7**, 10628 (2016).

[20] H. K. Xu, C. Song, W. Y. Liu, G. M. Xue, F. F. Su, H. Deng, Ye Tian, D. N. Zheng, S. Han, Y. P. Zhong, H. Wang, Y.-x. Liu, and S. P. Zhao, Nat. Commun. **7**, 11018 (2016).

[21] I.-C. Hoi, C. M. Wilson, G. Johansson, J. Lindkvist, B. Peropadre, T. Palomaki, and P. Delsing, New J. Phys. **15**, 025011 (2013).

[22] B. Suri, Z. K. Keane, R. Ruskov, L. S. Bishop, C. Tahan, S. Novikov, J. E. Robinson, F. C. Wellstood, and B. S. Palmer, New J. Phys. **15**, 125007 (2013).

[23] S. Novikov, T. Sweeney, J. E. Robinson, S. P. Premaratne, B. Suri, F. C. Wellstood, and B. S. Palmer, Nat. Phys. **12**, 75 (2016).

[24] C.-P. Yang, Q.-P. Su, S.-B. Zheng, and S. Han, Phys. Rev. A **87**, 022320 (2013).

[25] Z. H. Peng, Yu-xi Liu, J. T. Peltonen, T. Yamamoto, J. S. Tsai, and O. Astafiev, Phys. Rev. Lett. **115**, 223603 (2015).

[26] M. Hua, M.-J. Tao, and F.-G. Deng, Phys. Rev. A **90**, 012328 (2014).

[27] X.-L. He, C.-P. Yang, S. Li, J.-Y. Luo, and S. Han, Phys. Rev. A **82**, 024301 (2010).

[28] W. Qin, X. Wang, A. Miranowicz, Z. Zhong, and F. Nori, Phys. Rev. A **96**, 012315 (2017).

[29] H. Wang, M. Mariantoni, R. C. Bialczak, M. Lenander, E. Lucero, M. Neeley, A. D. O'Connell, D. Sank, M. Weides, J. Wenner, T. Yamamoto, Y. Yin, J. Zhao, J. M. Martinis, and A. N. Cleland, Phys. Rev. Lett. **106**, 060401 (2011).

[30] S. Berger, M. Pechal, S. Pugnetti, A. A. Abdumalikov, Jr., L. Steffen, A. Fedorov, A. Wallraff, and S. Filipp, Phys. Rev. B **85**, 220502 (2012).

[31] C. Neill, P. Roushan, K. Kechedzhi, S. Boixo, S. V. Isakov, V. Smelyanskiy, R. Barends, B. Burkett, Y. Chen,

Z. Chen, B. Chiaro, A. Dunsworth, A. Fowler, B. Foxen, R. Graff, E. Jeffrey, J. Kelly, E. Lucero, A. Megrant, J. Mutus, M. Neeley, C. Quintana, D. Sank, A. Vainsencher, J. Wenner, T. C. White, H. Neven, and J. M. Martinis, arXiv:1709.06678.

[32] Z. Chen, J. Kelly, C. Quintana, R. Barends, B. Campbell, Yu Chen, B. Chiaro, A. Dunsworth, A. G. Fowler, E. Lucero, E. Jeffrey, A. Megrant, J. Mutus, M. Neeley, C. Neill, P. J. J. O'Malley, P. Roushan, D. Sank, A. Vainsencher, J. Wenner, T. C. White, A. N. Korotkov, and J. M. Martinis, Phys. Rev. Lett. **116**, 020501 (2016).

[33] D. Sank, Z. Chen, M. Khezri, J. Kelly, R. Barends, B. Campbell, Y. Chen, B. Chiaro, A. Dunsworth, A. Fowler, E. Jeffrey, E. Lucero, A. Megrant, J. Mutus, M. Neeley, C. Neill, P. J. J. O'Malley, C. Quintana, P. Roushan, A. Vainsencher, T. White, J. Wenner, A. N. Korotkov, and J. M. Martinis, Phys. Rev. Lett. **117**, 190503 (2016).

[34] J. M. Martinis, S. Nam, J. Aumentado, and C. Urbina, Phys. Rev. Lett. **89**, 117901 (2002).

[35] The sample is similar to the one used in Ref. [20].

[36] Y. Tian, H. F. Yu, H. Deng, G. M. Xue, D. T. Liu, Y. F. Ren, G. H. Chen, D. N. Zheng, X. N. Jing, Li Lu, S. P. Zhao, and S. Han, Rev. Sci. Instrum. **83**, 033907 (2012).

[37] H. F. Yu, X. B. Zhu, Z. H. Peng, W. H. Cao, D. J. Cui, Y. Tian, G. H. Chen, D. N. Zheng, X. N. Jing, Li Lu, S. P. Zhao, and S. Han, Phys. Rev. B **81**, 144518 (2010).

[38] H. F. Yu, X. B. Zhu, Z. H. Peng, Ye Tian, D. J. Cui, G. H. Chen, D. N. Zheng, X. N. Jing, Li Lu, S. P. Zhao, and S. Y. Han, Phys. Rev. Lett. **107**, 067004 (2011).

[39] R. C. Bialczak, Development of the fundamental components of a superconducting qubit quantum computer, Ph.D. thesis, University of California, Santa Barbara, 2011.

[40] We have simplified the notations using $\gamma_{\varphi 1} = \gamma_{10}^{\varphi}$ and $\gamma_{\varphi 2} = \gamma_{20}^{\varphi}$.

[41] We note that the low-frequency flux noise induced dephasing rate γ_{j0}^{φ} is proportional to $d\omega_{j0}(\Phi)/d\Phi$ ($j = 1,2$) where Φ is the flux bias. Since the proportionality constant is determined by the integrated flux noise, which is the same for all values of j, and can be estimated from the measured γ_{10}^{φ} and $d\omega_{10}(\Phi)/d\Phi$, we were able to estimate γ_{20}^{φ} from the measured $d\omega_{20}(\Phi)/d\Phi$ and the known proportionality constant.